

Mid-wavelength infrared heterojunction phototransistors based on type-II InAs/AlSb/GaSb superlattices

A. Haddadi, S. Adhikary, A. Dehzangi, and M. Razeghi

Citation: *Appl. Phys. Lett.* **109**, 021107 (2016); doi: 10.1063/1.4958715

View online: <http://dx.doi.org/10.1063/1.4958715>

View Table of Contents: <http://aip.scitation.org/toc/apl/109/2>

Published by the [American Institute of Physics](#)

Mid-wavelength infrared heterojunction phototransistors based on type-II InAs/AlSb/GaSb superlattices

A. Haddadi, S. Adhikary, A. Dehzangi, and M. Razeghi^{a)}

Center for Quantum Devices, Department of Electrical Engineering and Computer Science, Northwestern University, Evanston, Illinois 60208, USA

(Received 13 February 2016; accepted 28 June 2016; published online 12 July 2016)

A mid-wavelength infrared heterojunction phototransistor based on type-II InAs/AlSb/GaSb superlattices on GaSb substrate has been demonstrated. Near a wavelength of $4\ \mu\text{m}$ saturated optical gains of 668 and 639 at 77 and 150 K, respectively, are demonstrated over a wide dynamic range. At 150 K, the unity optical gain collector dark current density and DC current gain are $1 \times 10^{-3}\ \text{A}/\text{cm}^2$ and 3710, respectively. This demonstrates the potential for use in high-speed applications. In addition, the phototransistor exhibits a specific detectivity value that is four times higher compared with a state-of-the-art type-II superlattice-based photodiode with a similar cut-off wavelength at 150 K.

Published by AIP Publishing. [<http://dx.doi.org/10.1063/1.4958715>]

Rapidly growing use of the Internet and multimedia services has created congestion in the telecommunications networks and placed many new requirements on carriers. Customers want ultra-high-speed, multi-gigabit-per-second (multi-Gb/s) bandwidth, which is traditionally accomplished using optical fibers. However, installing new fiber optic cable to all customers is prohibitively expensive, especially in metropolitan areas. Free-space optical (FSO) communication is considered to be one of the key technologies for supplying high-bandwidth, “last-mile” connections to customers without the need for optical fiber.¹ Using lasers as signal carriers, FSO laser communications (Laser-Com) can provide a line-of-sight, wireless, high-bandwidth, communication link between remote sites. FSO Laser-Com offers substantial advantages over conventional RF wireless communications technology, including higher data rates, low probability of intercept, low power requirements, and much smaller packaging.^{2,3} FSO Laser-Com systems have proven to be a viable alternative to optical fiber based systems in several applications, as the technology comes closer and closer to providing the 5-nines (99.999%) service that many different types of users require from their data networks.

The current state-of-the-art in FSO communications is based around near-infrared (NIR, $0.8 < \lambda < 2\ \mu\text{m}$) sources and photodetectors. Thanks to extensive development for near-infrared for commercial optical fiber communications, this technology is readily available at low costs. Within the NIR spectral range, however, a major concern is the eye safety of the lasers. These wavelengths can transmit directly through the cornea and, at high power, cause damage to the retina.

NIR FSO communication is also hampered by atmospheric scattering and absorption. Moving from the NIR towards the mid-wavelength infrared (MWIR, $3 < \lambda < 5\ \mu\text{m}$) allows superior transmission through common atmospheric problems such as fog, clouds, and smoke. When coupled with improvements in MWIR laser and modulator design,⁴⁻⁶ this makes possible reliable optical replacements for radio,

microwave, and even NIR FSO communications links in many applications. This is driving a new demand for fast and sensitive MWIR photodetectors suitable for FSO communication. However, photodetector performance in the MWIR region is still behind the requirements of FSO communications. Achieving suitable performance will require developing a novel solution that can overcome current device limitations.

To date, most NIR optical receiver designs have employed *pin* photodiodes as photodetectors. However, these devices exhibit no internal/intrinsic gain, and the increased capacitance due to their relatively large-area intrinsic absorption layer is known to be the limiting factor for high frequency operation of the photoreceiver. Metal-semiconductor-metal (MSM) photodetectors, on the other hand, have low capacitance due to their Schottky contacts which make them suitable for high frequency operation but their temperature instability, lack of internal gain, and complicated epitaxial growth and fabrication processes limit their use for MWIR optical receivers.

Heterojunction phototransistors (HPTs) are an alternative technology that can demonstrate both high speed and internal gain.⁷⁻¹¹ Functionally, a HPT is a *pin* photodiode integrated with a bipolar transistor to form an integrated amplifier.⁸ Unlike avalanche photodiodes (APDs),^{12,13} HPTs can provide large photocurrent gain without requiring high bias voltages or the excess avalanche noise characteristic of avalanche photodiode operation.¹⁴ Furthermore, HPTs are well suited to integration with heterojunction bipolar transistors in receivers or other circuits.¹⁵ It is, therefore, expected that HPTs will provide an exciting alternative for the manufacture of MWIR optical receivers for FSO communication and high-sensitivity MWIR imagers.

Most of the HPTs reported in the literature are based on InGaAs compounds that provide limited cut-off wavelength tunability and are limited to the NIR spectral region.^{2,9} In contrast, type-II superlattices^{16,17} (T2SLs) are a developing material system with intrinsic advantages such as great flexibility in bandgap engineering, low growth and manufacturing cost, high-uniformity,¹⁸ Auger recombination suppression,¹⁹ and high carrier effective mass.²⁰ As such,

^{a)} Author to whom correspondence should be addressed. Electronic mail: razeghi@eecs.northwestern.edu

T2SLs are becoming an attractive candidate for infrared detection and imaging¹⁷ from the short-wavelength infrared (SWIR) to the very long wavelength infrared (VLWIR) regime.^{21–23} In this paper, we report the demonstration of a MWIR HPT based on type-II superlattices. Such devices can be used for making both MWIR FSO systems and high-speed sensitive MWIR imagers.

An *npn* HPT structure was chosen to be used in this study. The device consists of a *n*-doped M-structure-based²⁰ wide-bandgap emitter, a *p*-doped T2SL-based base, and a lightly doped *n*-type T2SL-based collector. The emitter superlattice design consists of 7/1/5/1 mono-layers (MLs) of InAs/GaSb/AlSb/GaSb, respectively, per period with a ~ 650 meV bandgap at 77 K. The base and collector regions share the same design which consists of 6.5 MLs of InAs and 12 MLs of GaSb per period²⁴ with one binary InSb interface and the other interface being InGaSb to reduce the mismatch. This superlattice has a ~ 310 meV bandgap at 77 K.

The incident MWIR light is absorbed in the T2SL-based base and collector regions, creating electron-hole pairs. In this device, the collector region is completely depleted; therefore, drift is the main transport mechanism inside the collector region that helps faster transfer of photo-generated holes from the collector region to the base region. The photo-generated holes accumulate in the base and alter the base-emitter potential so that electrons are injected from the emitter into the base, i_{nE} , and, subsequently, enter the collector region.⁸ Current gain in this device is achieved by normal transistor action when the base width, w_B , is less than the diffusion length, L_n , of the injected electrons (see Figure 1). The function of the wide-bandgap emitter is to increase the emitter injection efficiency by preventing reverse injection of holes from the base into the emitter.⁸

The material for this study was grown using a GEN II molecular beam epitaxy (MBE) reactor, equipped with group-III SUMO[®] cells and group-V valved crackers, on a Tellurium-doped (10^{18} cm⁻³) *n*⁺-GaSb substrate. The growth was started with a 100 nm GaSb layer followed by a 0.5 μ m *n*-doped InAs_{0.91}Sb_{0.09} buffer layer (10^{18} cm⁻³). The device structure was started by growing an *n*-type (10^{18} cm⁻³) 0.5 μ m-thick contact layer. The contact layer

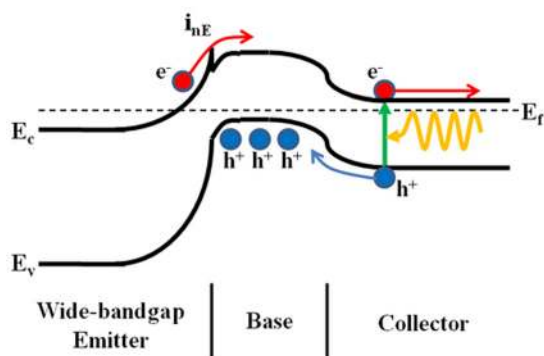


FIG. 1. Energy-band diagram of the MWIR heterojunction phototransistor. The incident light is absorbed in the T2SL-based base and collector regions, creating electron-hole pairs. The photo-generated holes accumulate in the base region and alter the base-emitter potential so that electrons are injected from the emitter into the base region. Current gain is achieved by normal transistor action when the base width is less than the diffusion length of the injected electrons.

superlattice design is the same as the emitter region. Then, the 0.5 μ m-thick wide-bandgap *n*-doped ($\sim 10^{17}$ cm⁻³) emitter was grown. This was followed by growing a 60 nm-thick *p*-doped base layer ($\sim 6 \times 10^{16}$ cm⁻³), a 1 μ m-thick *n*-doped collector/absorption region ($\sim 5 \times 10^{15}$ cm⁻³), and a 500 nm *p*-type top contact (10^{18} cm⁻³). The base, collector, and top contact regions share the same superlattice design. Silicon (Si) and beryllium (Be) were used as the *n*- and *p*-type dopants, respectively.

After the epitaxial growth, the material quality was assessed using high resolution X-ray diffraction (HR-XRD) and atomic force microscopy (AFM). The satellite peaks in the HR-XRD scan showed thicknesses of 49 and 62 Å for the period of the emitter and base/collector regions, respectively, which agrees well with the designed values of 49 and 62.5 Å at room temperature. The lattice mismatch between both superlattice designs and the GaSb substrate was less than 1000 ppm, as expected. The AFM showed a good surface morphology with well-ordered atomic steps and a root mean squared (RMS) roughness of 1.23 Å over a $10 \times 10 \mu\text{m}^2$ area.

The grown sample was processed into a set of unpassivated mesa-isolated test structures with device sizes ranging from 100×100 to $400 \times 400 \mu\text{m}^2$ using standard photolithographic processing techniques which were used for T2SL-based photodetectors.²⁵ The phototransistors were left unpassivated but carefully treated, by performing many surface cleaning steps, in order to minimize the surface leakage. Then, the sample was wire-bonded to a 68 pin leadless ceramic chip carrier (LCCC). The emitter and collector terminals of each device were wire-bonded while the base terminal was left floating. For simplicity, in the rest of this paper, we will refer to the collector-emitter bias voltage, V_{CE} , as the applied bias voltage. Finally, the sample was loaded into a cryostat for both electrical and optical characterization at 77 and 150 K.

The optical characterization was done in front-side illumination configuration without applying any anti-reflection (AR) coating to the phototransistors. A Bruker IFS 66v/S Fourier transform infrared spectrometer (FTIR) was used to measure the spectral response of the phototransistor. The absolute responsivity of the phototransistor was measured with a calibrated blackbody source at 1000 °C. The optical performance of the devices is shown in Figure 2. The device exhibits a 50% cut-off wavelength of $\sim 3.95 \mu\text{m}$ at 77 K as predicted from the band structure calculations. The device responsivity reaches a peak value of 1960 A/W around 3.6 μm under 680 mV applied bias for a 1 μm -thick collector/absorption region at 77 K. At 150 K, the device shows a 50% cut-off wavelength of $\sim 4.05 \mu\text{m}$. The device responsivity reaches a peak of 2152 A/W around 3.6 μm under 400 mV applied bias. The peak responsivity starts to saturate under bias voltages higher than 600 and 300 mV at 77 and 150 K, respectively. At higher bias voltages, the combination of the dark current and photocurrent becomes higher than the input current limit of our transimpedance amplifier; thus, we performed optical characterization up to 680 and 400 mV applied bias voltages at 77 and 150 K, respectively.

Figure 3 presents the results of the optical gain measurements at 3.6 μm . The optical gain of the phototransistor is the ratio of the number of photo-generated carriers creating

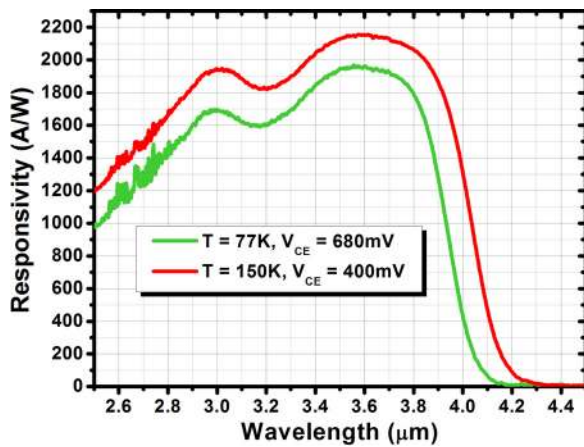


FIG. 2. Saturated responsivity spectrum of the device at 77 K under 680 mV applied bias (V_{CE}) and at 150 K under 400 mV applied bias in front-side illumination configuration without any anti-reflection coating.

the photocurrent to the number of incident photons. In order to study the variation of optical gain versus applied bias, the same calibrated blackbody source at 1000 °C was used. At 77 K, the device optical gain becomes unity under 200 mV applied bias (see Figure 3(a)). The optical gain increases with increasing applied bias and reaches its saturation value of 668 at bias voltages higher than ~ 600 mV. In contrast, the device optical gain becomes unity at 150 K under 110 mV applied bias. The optical gain at this operating temperature saturates at bias voltages higher than 350 mV. The saturated optical gain at 150 K is 639. Unlike existing avalanche photodiodes (APDs) that show an exponential relation between their optical gain and applied bias, this device shows better tolerance to variation in applied bias voltage. Moreover, this device does not require high bias voltages (several volts), like APDs; this will make it much easier to integrate our device with commercial CMOS components.

In order to study the effect of incoming optical power on the device optical gain, we swept the blackbody temperature from 1000 °C down to 50 °C and measured the optical gain under 680 and 400 mV applied biases at 77 and 150 K operating temperatures, respectively. Figures 3(b) and 3(c) present the optical gain of the device versus the blackbody temperature. The device shows very small gain change over a broad range of optical power in which reveals a high dynamic range.

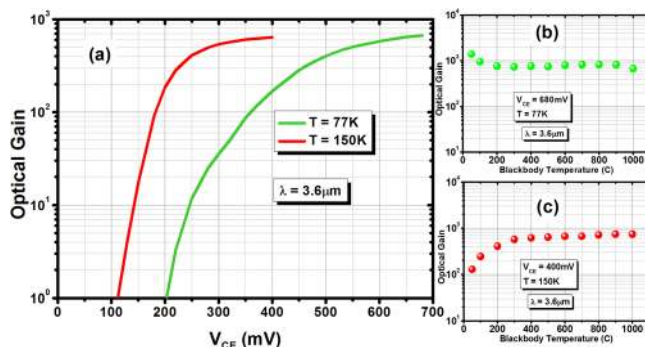


FIG. 3. (a) The device optical gain around 3.6 μm variation vs. applied bias at 77 K and 150 K. The device optical gain around 3.6 μm vs. blackbody temperature/optical power density (b) at 77 K and (c) 150 K.

Figure 4 presents the collector dark current density (J_C) versus applied bias voltage. At 77 K, the sample exhibits a unity optical gain collector dark current density of 1.8×10^{-6} A/cm² under 200 mV applied bias, whereas at 150 K, the unity optical gain collector dark current density at 110 mV is 1×10^{-3} A/cm². The variation of the inverse of the $R \times A$ (at 600 mV) with the perimeter over area ratio (not shown here) proved that surface leakage is the main source of the dark current in our devices. In order to calculate the DC current gain (β) of the phototransistor, a photodiode with the same absorption region design and thickness (1 μm) was grown and optically characterized. Its responsivity value was 0.5 and 0.58 A/W around 3.6 μm at 77 and 150 K, respectively; this provides an estimate of the generated photocurrent inside the collector region. One can calculate the DC current gain by dividing the phototransistor responsivity into the photodiode responsivity at the same wavelength (in this case around 3.6 μm). The device exhibits a saturated DC current gain of 3881 and 3710 at 77 and 150 K, respectively. The DC current gain relation with applied bias is similar to the optical gain relation with the applied bias that was presented before (see Figure 3(a)). Considering high DC current gain, one can increase the optical response by using a thicker collector region in order to improve the sensitivity of the device.

After performing both optical and electrical characterizations, the specific detectivity (D^*) was calculated for the phototransistor at 77 and 150 K. The device exhibits a saturated dark current shot noise limited specific detectivity of 1.1×10^{13} cm \cdot Hz^{1/2}/W under 500 mV of applied bias at 77 K (Figure 5(a)) for a fully immersed 300 K background with a 2π field-of-view (FOV). At 150 K, the device exhibits a specific detectivity of 4.4×10^{12} cm \cdot Hz^{1/2}/W under 280 mV applied bias (Figure 5(a)) for the same background condition. Figure 5(a) also shows a comparison between the specific detectivity values of the phototransistor at 77 and 150 K with a state-of-the-art T2SL-based heterojunction photodiode²³ operating at 150 K. The phototransistor exhibits a specific detectivity value that is four times higher than the photodiode at 150 K. Moreover, the phototransistor generates more photo-current than the photodiode for the same incoming optical power (2–3 orders of magnitude) which can be used for

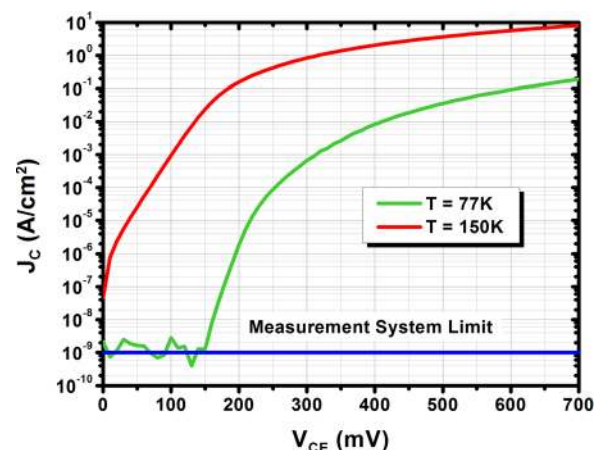


FIG. 4. Collector dark current density vs. applied bias voltage characteristic of the device at 77 K and 150 K.

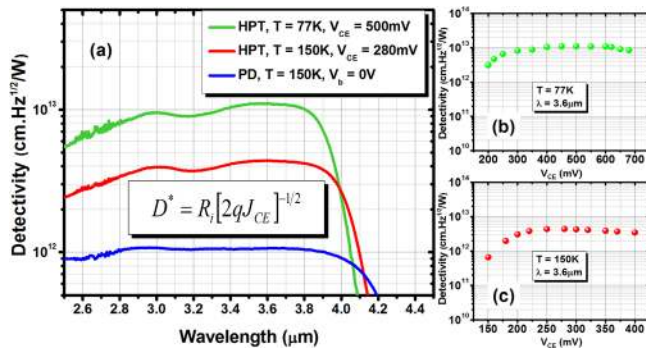


FIG. 5. (a) Specific detectivity (D^*) spectrum comparison between heterojunction phototransistor (HPT) operating at 77 and 150 K with a T2SL-based MWIR heterojunction photodiode (PD) operating at 150 K in front-side illumination configuration without any anti-reflection coating. Specific detectivity of the phototransistor around $3.6 \mu\text{m}$ versus applied bias voltage at (b) 77 K and (c) 150 K. The specific detectivity is calculated based on the equation in the inset, where R_i is the device responsivity, J_{CE} is the collector dark current density, and q is the fundamental charge.

making imagers hundreds of times faster and more sensitive than current photodiode-based imagers.

Figures 5(b) and 5(c) show the phototransistor specific detectivity variation versus applied bias around $3.6 \mu\text{m}$ at 77 and 150 K, respectively. The specific detectivity stays relatively constant for a broad range of applied biases at both operating temperatures. Therefore, this device can be used at lower bias voltages without reducing the specific detectivity for applications that need lower dark current density and lower optical gain. In addition, the specific detectivity spectrum stays almost constant over a broad range of wavelengths (Figure 5(a)), which makes this phototransistor a promising choice for MWIR infrared imaging applications.

In this paper, we have reported the design, growth, and characterization of MWIR heterojunction phototransistors (HPTs) based on type-II InAs/AlSb/GaSb superlattices on GaSb substrate. The devices exhibited 50% cut-off wavelengths of ~ 3.95 and $\sim 4.05 \mu\text{m}$ at 77 and 150 K, respectively. A saturated optical gain of 668 and 639 at 77 and 150 K, respectively, was measured. At 150 K, the unity optical gain collector dark current density and DC current gain are $1 \times 10^{-3} \text{ A/cm}^2$ and 3710, respectively. Also at 150 K, the device exhibited a specific detectivity of $4.4 \times 10^{12} \text{ cm}\cdot\text{Hz}^{1/2}/\text{W}$, which stays constant over a broad range of wavelengths and applied biases. This specific detectivity value is four times higher than a state-of-the-art T2SL-based photodiode with a similar cut-off wavelength. In conclusion, this work has shown that it is possible to create high performance gain-based MWIR photodetectors based on type-II InAs/AlSb/GaSb superlattices. Thanks to the extreme bandstructure

tunability of this material system, T2SL-based HPTs can help facilitate development of high-speed free-space optical communication systems in the MWIR region as well as better MWIR imagers (compared with those based on conventional photodiodes).

- ¹A. Pavelchek, R. G. Trissel, J. Plante, and S. Umbrasas, "Long-wave infrared ($10\text{-}\mu\text{m}$) free-space optical communication system," *Proc. SPIE* **5160**, 247 (2004).
- ²J. M. Kahn, "Secure free-space optical communication between moving platforms," in *The 15th Annual Meeting of the IEEE Lasers and Electro-Optics Society (LEOS 2002)* (IEEE, 2002), Vol. 452, p. 455.
- ³J. R. Minch, D. R. Gervais, and D. J. Townsend, "Adaptive Transceivers for Mobile Free-Space Optical Communications," in *2006 IEEE Military Communications Conference (MILCOM 2006)* (IEEE, 2006), pp. 1–5.
- ⁴E. Luzhanskiy, F.-S. Choa, S. Merritt, A. Yu, and M. Krainak, *Comparative Analysis of QCL MWIR and SWIR Communication with PPM Signals*, Arlington, Virginia (Optical Society of America, 2015), Paper No. JT5A.7.
- ⁵A. Hood, A. Evans, and M. Razeghi, "Type-II superlattices and quantum cascade lasers for MWIR and LWIR free-space communications," *Proc. SPIE* **6900**, 690005 (2008).
- ⁶E. Luzhanskiy, F.-S. Choa, S. Merritt, A. Yu, and M. Krainak, "Mid-IR free-space optical communication with quantum cascade lasers," *Proc. SPIE* **9465**, 946512 (2015).
- ⁷F. Capasso, W. T. Tsang, C. G. Bethea, A. L. Hutchinson, and B. F. Levine, *Appl. Phys. Lett.* **42**, 93 (1983).
- ⁸J. C. Campbell and K. Ogawa, *J. Appl. Phys.* **53**, 1203 (1982).
- ⁹L. Y. Leu, J. T. Gardner, and S. R. Forrest, *J. Appl. Phys.* **69**, 1052 (1991).
- ¹⁰V. Fathipour, O. G. Memis, S. J. Jang, R. L. Brown, I. H. Nia, and H. Mohseni, *IEEE J. Sel. Top. Quantum Electron.* **20**, 65 (2014).
- ¹¹V. Fathipour, S. J. Jang, I. H. Nia, and H. Mohseni, *Appl. Phys. Lett.* **106**, 021116 (2015).
- ¹²S. Mallick, K. Banerjee, S. Ghosh, E. Plis, J. B. Rodriguez, S. Krishna, and C. Grein, *Appl. Phys. Lett.* **91**, 241111 (2007).
- ¹³K. Banerjee, S. Ghosh, S. Mallick, E. Plis, S. Krishna, and C. Grein, *Appl. Phys. Lett.* **94**, 201107 (2009).
- ¹⁴O. G. Memis, A. Katsnelson, S.-C. Kong, H. Mohseni, M. Yan, S. Zhang, T. Hossain, N. Jin, and I. Adesida, *Opt. Express* **16**, 12701 (2008).
- ¹⁵H. Kamitsuna, Y. Matsuoka, S. Yamahata, and N. Shigekawa, *IEEE Trans. Microwave Theory Tech.* **49**, 1921 (2001).
- ¹⁶G. A. Sai-Halasz, R. Tsu, and L. Esaki, *Appl. Phys. Lett.* **30**, 651 (1977).
- ¹⁷M. Razeghi, U.S. patent 6864552 (2005).
- ¹⁸N. Binh-Minh, C. Guanxi, H. Minh-Anh, and M. Razeghi, *IEEE J. Quantum Electron.* **47**, 686 (2011).
- ¹⁹G. G. Zegrya and A. D. Andreev, *Appl. Phys. Lett.* **67**, 2681 (1995).
- ²⁰B.-M. Nguyen, D. Hoffman, P.-Y. Delaunay, E. K.-W. Huang, M. Razeghi, and J. Pellegrino, *Appl. Phys. Lett.* **93**, 163502 (2008).
- ²¹Y. Wei, J. Bae, A. Gin, A. Hood, M. Razeghi, G. J. Brown, and M. Tidrow, *J. Appl. Phys.* **94**, 4720 (2003).
- ²²Y. Wei, A. Gin, M. Razeghi, and G. J. Brown, *Appl. Phys. Lett.* **81**, 3675 (2002).
- ²³A. M. Hoang, G. Chen, A. Haddadi, S. Abdollahi Pour, and M. Razeghi, *Appl. Phys. Lett.* **100**, 211101 (2012).
- ²⁴S. A. Pour, E. K. Huang, G. Chen, A. Haddadi, B.-M. Nguyen, and M. Razeghi, *Appl. Phys. Lett.* **98**, 143501 (2011).
- ²⁵A. Hood, D. Hoffman, B.-M. Nguyen, P.-Y. Delaunay, E. Michel, and M. Razeghi, *Appl. Phys. Lett.* **89**, 093506 (2006).